Electronic Supplementary Material (ESI) for Journal of Materials Chemistry A.

Supporting Information

Thionated Benzo[*c*]thiophen-1(*3H*)-one as Organic Cathodes with High Capacity for Sulfur-rich All Organic Lithium-ion Battery

Bingjie Zhang,[a] XiaoDong Yang,[a] Ben He,[a] Qiqi Wang,[a] Zishun Liu,[b] Demei Yu,[a]* Gang He[a,b,c]*

[a] School of Chemistry jointly with Frontier Institute of Science and Technology, Xi'an Key Laboratory of Sustainable Energy Materials Chemistry.

[b] International Centre for Applied Mechanics, State Key Laboratory for Strength and Vibration of Mechanical Structures, School of Aerospace. Xi'an Jiaotong University, Xi'an, Shaanxi Province, 710049 (China)

[c] Guangdong Provincial Key Laboratory of Luminescence from Molecular Aggregates (South China University of Technology), Guangzhou 510640, (China)

E-mail: ganghe@mail.xjtu.edu.cn.

Abstract: Organic materials have potential advantages in lithium-ion batteries (LIBs) due to their environmental friendliness, flexible designability, and high theoretical capacity. However, the commonly low electrical conductivity and high solubility of conventional organic materials limit their further applications. Herein, we report a novel type of thiocarbonyl material, Benzo[c]thiophen-1(3*H*)-thione (**DPTTO**), which is based on a thionation strategy by substituting oxygen atoms with sulfur ones in benzo[c]thiophen-1(3*H*)-one (**DPTO**). **DPTTO** displays better comprehensive battery performance than **DPTO** with initial specific capacity of 162 mAh g^{-1} and long-life performance of 80 mAh g^{-1} at 1 A g^{-1} after 500 cycles. *In situ* Raman, *ex situ* X-ray photoelectron spectroscopy (XPS) and density functional theory calculations are conducted to reveal the lithiation process which occurs between thiocarbonyl and thiophene sulfide. For the sulfur-rich all organic lithium-ion cells, the average capacity is 75 mA h g^{-1} during 100 cycles (100 mA g^{-1}), which inspiring the exploration of the sulfur-rich organic materials for the future LIBs.

Table of Context

Experimental Section

1. Characterization and Instrumentation

The reactions were performed using standard Schlenk flasks at Ar atmosphere. Tert-butyl ether (THF), xylene (mixture of isomers) and chlorobenzene were dried from benzophenone/sodium before use. Phthalic anhydride, $Na_2S·9H_2O$, carbon disulphide, Lawesson's Reagent and *o*-Phthalic anhydride were purchased from Energy Chemical Inc. Column chromatographic purification of organic products was accomplished by using 200−300 mesh silica gel. If no other special indicated, other solvents and reagents were used as commercially available without further purification. H spectrum (^{1}H-NMR) of **DPTO** and phthalic thioanhydride (PTA) was tested by Bruker Avance II (400 MHz) spectrometer in the solvents indicated; solid-state MAS ^{13}C-NMR of **DPTTO** was obtained by Bruker AVANCE 400 (SB) spectrometer operating at a static magnetic field of 9.4T; chemical shifts are reported in units (ppm) by assigning TMS resonance in the ^{1}H spectrum as 0.00 ppm and $CDCl_3$ resonance in the ^{13}C spectrum as 77.00 ppm. Coupling constants are reported in Hz with multiplicities denoted as s (singlet), d (doublet), t (triplet), q (quartet) and m (multiplet). Fourier transform infrared spectroscopy (FTIR) was recorded by Nicolet 6700 FT-IR Instrument. The electrical conductivities were measured by a semiconductor analyzer (Keithley 2400) in a two-probe configuration. Raman measurements were performed on a HORIBA Laser Raman Spectrometer using 325 and 532 nm diode-pumped solid-state laser, attenuated to give ~100 mW power at the sample surface. Thermogravimetric analysis (TGA) test were put in a METTLER TOLEDO TGA/DSC^{3+} thermal analyzer under nitrogen gas, and the temperature range was from 30 to 700 °C with a heating rate of 10 K·min^{-1}. The mass spectrometry measurements were collected by a Bruker maxis MALDI-TOF mass spectrometer in electron spray ionization-positive mode. X-ray powder diffraction patterns were recorded on a SMARTLAB(3). X-ray photoelectron spectroscopy (XPS) were collected by the Thermo Fisher ESCALAB Xi$^+$.Photographs were taken with a Nikon D5100 digital camera.

2. Synthetic procedure

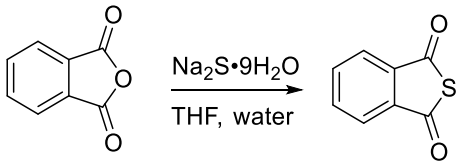

Scheme S1. General synthetic routes to the PTA.

The synthesis of PTA refers to the literature[1] with some improvements as follows: in a 500 mL round-bottomed flask equipped with a magnetic stir bar, phthalic anhydride (0.1 mol, 2.0 equiv) was dissolved into 200 mL THF, and the water solution of $Na_2S·9H_2O$ (0.05 mol, 1 equiv) was added to the solution at 25 °C and stirred for 10-30 min (monitored by TLC). THF was removed in vacuum, and aqueous phase was exacted with methyl tert-butyl ether for 3 times. Then, the organic phase was dried with Na_2SO_4. The crude PTA was collected after removing methyl tert-butyl ether, and then a further purification by sublimation at 85 °C. Yield: 99%. ^{1}H NMR (400 MHz, $CDCl_3$) δ 7.99–7.95 (m, 2H), 7.83–7.79 (m, 2H). ^{13}C NMR (100 MHz, $CDCl_3$) δ 189.28 (s), 138.61 (s), 135.08 (s), 123.75 (s).

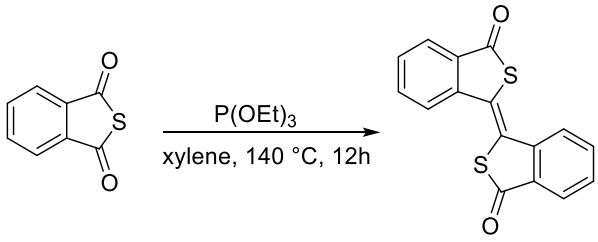

Scheme S2. General synthetic routes to the products **DPTO**.

The PTA (4.00 g, 24.0 mmol) and $P(OEt)_3$ (2.50 mL, 14.5 mmol) were both added in 15 mL xylene. The mixture solution was stirred under Ar atmosphere at 140 °C for overnight. After the solution was cooled to 25 °C, the brown yellow bulk was filtrated and washed with methanol three times. Next hen, the solid was passed through silica gel columns by using eluent of petroleum ether (PE)/dichloromethane (DCM) (25/1 to 5/1, v/v), followed by 3 recrystallizations from xylene to afford 0.63 g of dione yellow needle-like solid. Yield: 20%. ^{1}H-NMR (400 MHz, $CDCl_3$) δ (TMS, ppm): 8.35 (d, 2H, *J* = 12.0 Hz), 8.00 (d, 2H, *J* = 8.0 Hz), 7.81 (t, 2H, *J* = 8.0 Hz), 7.60 (t, 2H, *J* = 8.0 Hz). HR-ESI-MS: m/z calculated for $[M+H]^+$ $C_{16}H_9O_2S_2$: 297.0044; found: 297.0037.

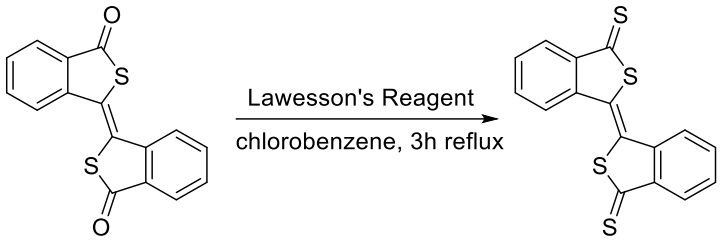

Scheme S3. General synthetic routes to the target products **DPTTO**.

A hot solution of **DPTO** (0.741 g, 0.025 mmol) in chlorobenzene (35 mL) was treated with Lawesson's reagent (1.2134 g, 0.04 mmol) and refluxed for 3 h. The crude product was filtered, washed with chlorobenzene, carbon disulfide and was refluxed with 80% ethanol to furnish **DPTTO** (0.521 mg). Solid-state ^{13}C NMR (400 MHz, 298K) δ(ppm): 145.65, 144.35, 139.88, 136.94, 116.75. MALDI-TOF-MS: m/z calculated for $[M+H]^+$ $C_{16}H_9S_2S_2$: 329.48; found: 329.01.

3. ^{1}H, ^{13}C NMR spectra and MALDI-TOF-MS

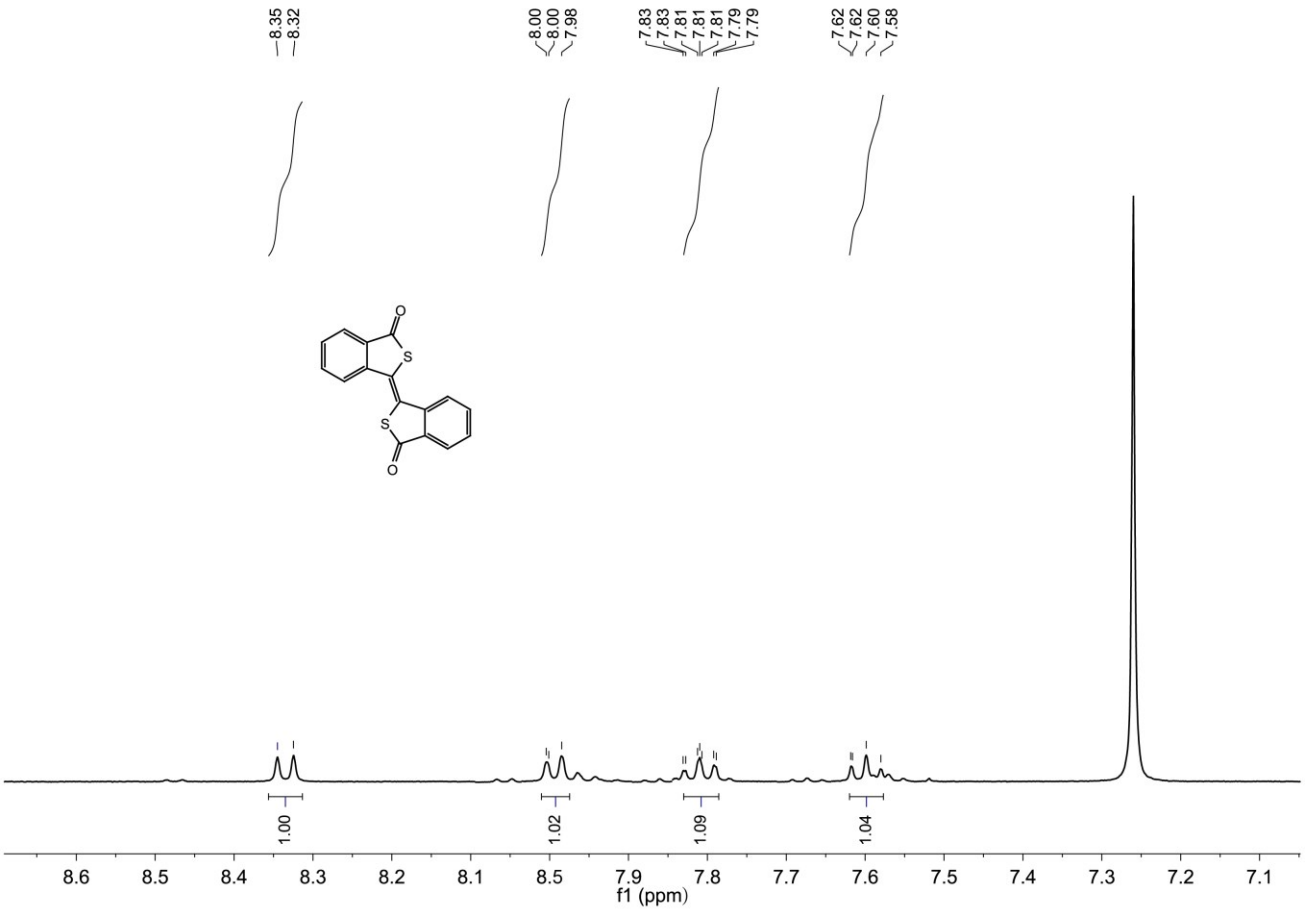

Figure S1. ^{1}H NMR spectrum of **DPTO** in deuterated chloroform.

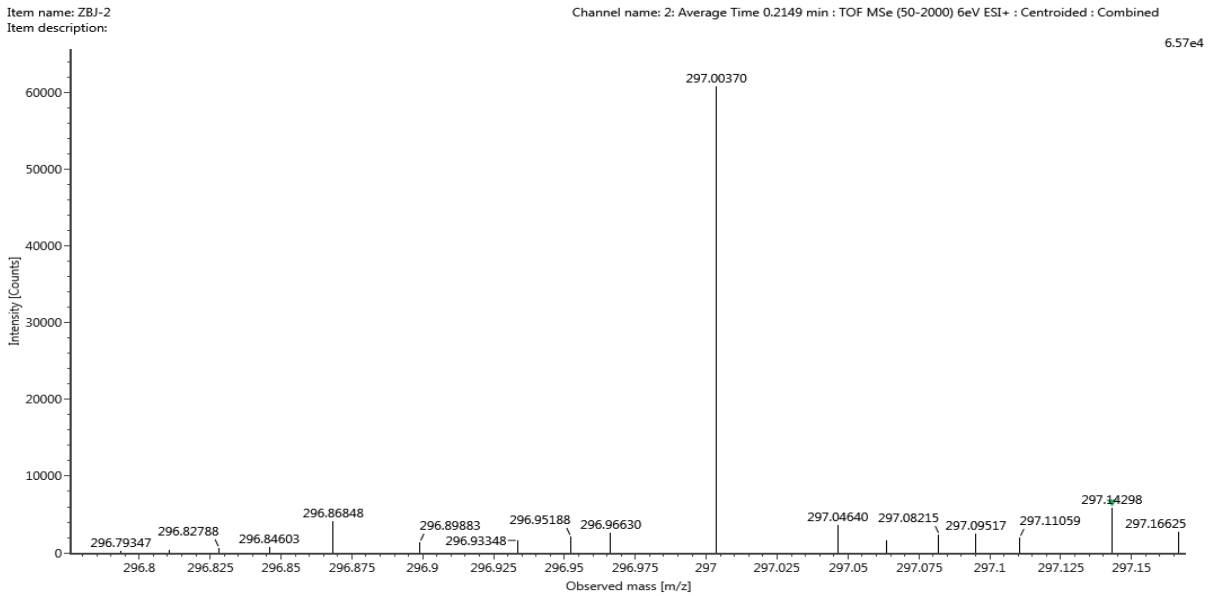

Figure S2. HR-MS spectrum for **DPTO**.

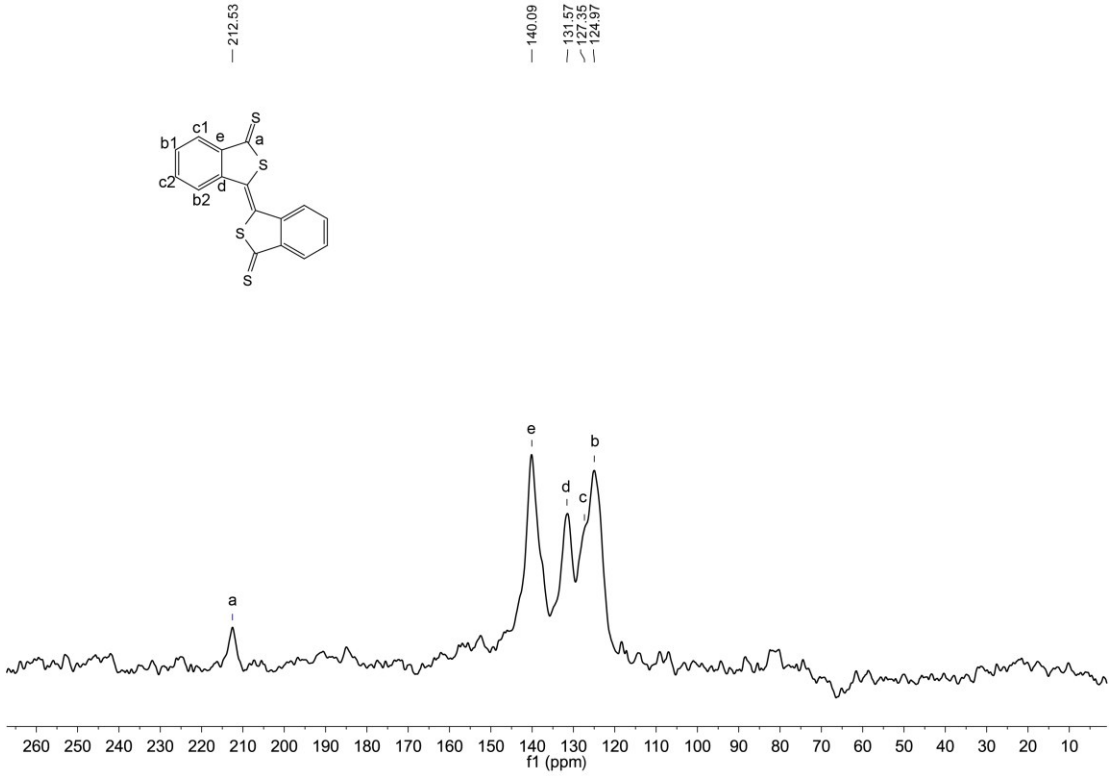

Figure S3. Solid-state MAS ^{13}C-NMR for **DPTTO**.

As **DPTTO** is hard to dissolve in any solvent, the solid-state ^{13}C NMR spectrum was obtained to determine its structure. Due to the strong polarization of these rigid rings, the spectral line is greatly widened. However, we can get the needed information from the five peaks between 120 and 220 ppm. From Spectral Database for Organic Compounds, **DPTTO**, the corresponding chemical shifts are as follows: δ a=212.53 ppm (2C), δ b1=δ b2=124.97 ppm (4C), δ c1=δ c2=127.35 ppm (4C), δ d =131.57 ppm (2C), δ e =140.05 ppm (2C). Based on this data, we can reasonably assign the characteristic bands carbon a, b, c, d, and e respectively. Particular comparison indicates that the ratio of the area of each band matches the number of carbon atoms deduced from above assignment. These results support proof for the formation of the target **DPTTO**.

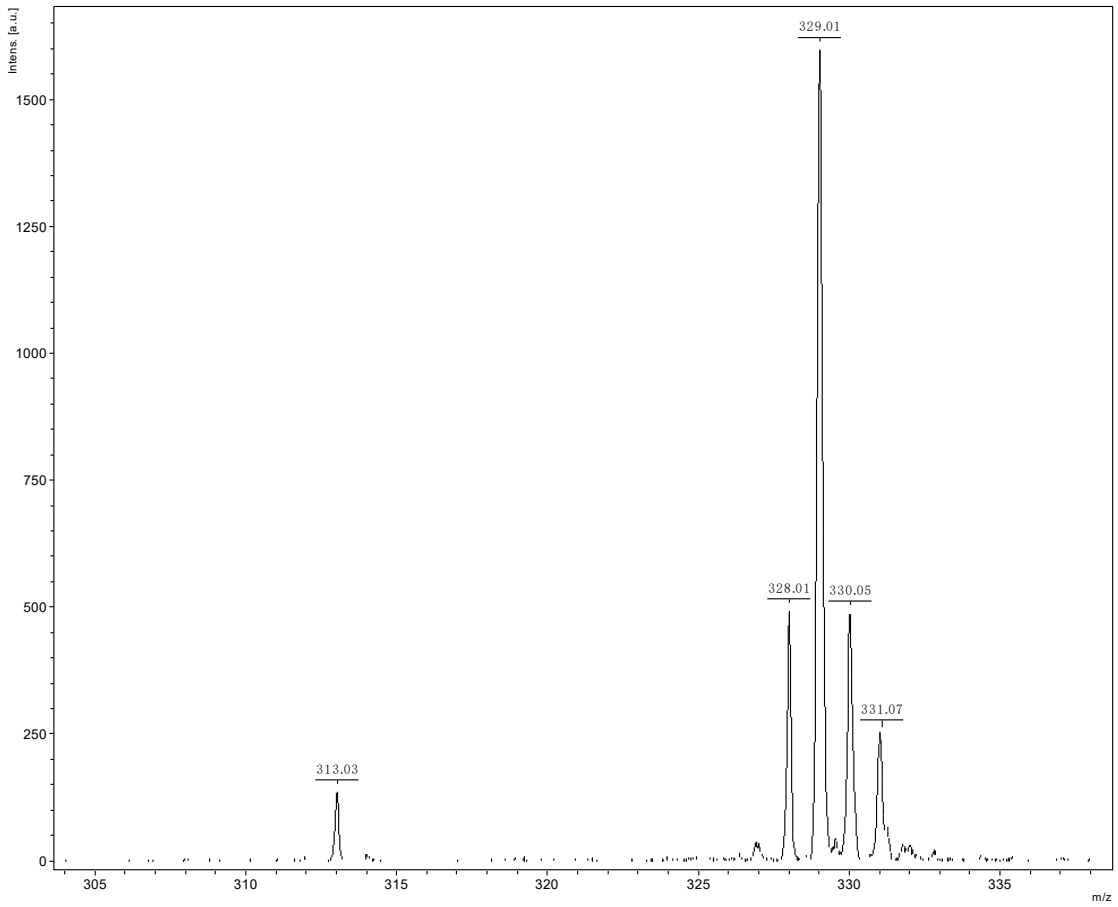

Figure S4. MALDI-TOF mass spectrometer was obtained to determine **DPTTO** mass.

4. FTIR spectra

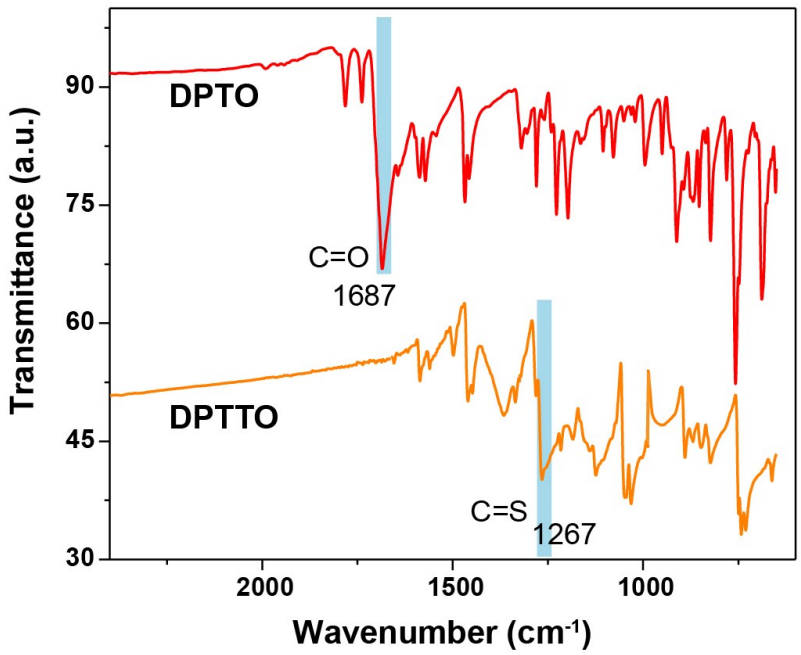

Figure S5. FT-IR spectra of **DPTO** and **DPTTO**

5. Raman curves

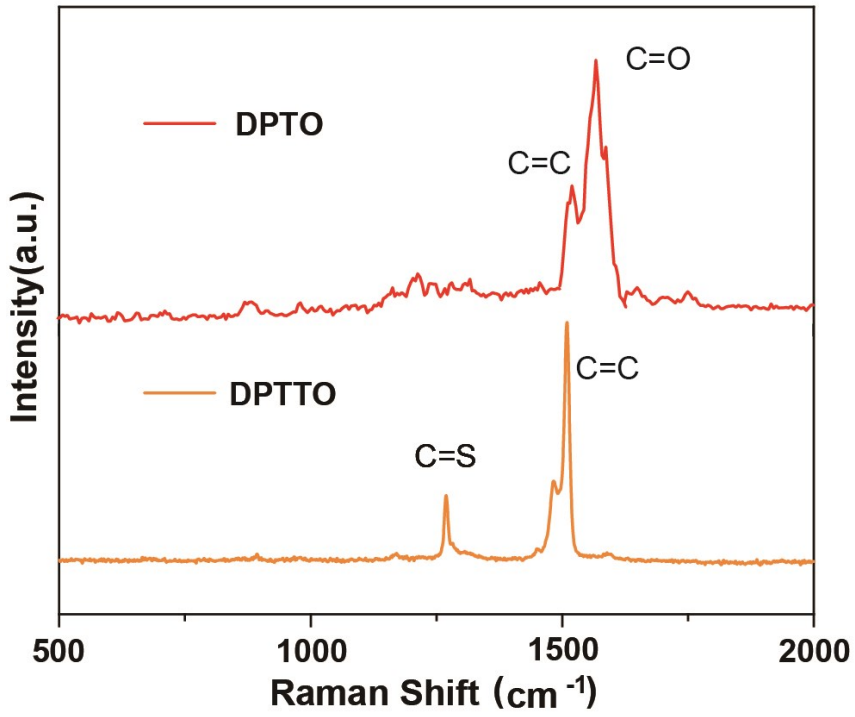

Figure S6. Raman plots of **DPTO** and **DPTTO** using 325 and 532 nm diode-pumped solid-state laser, respectively.

6. XRD curves

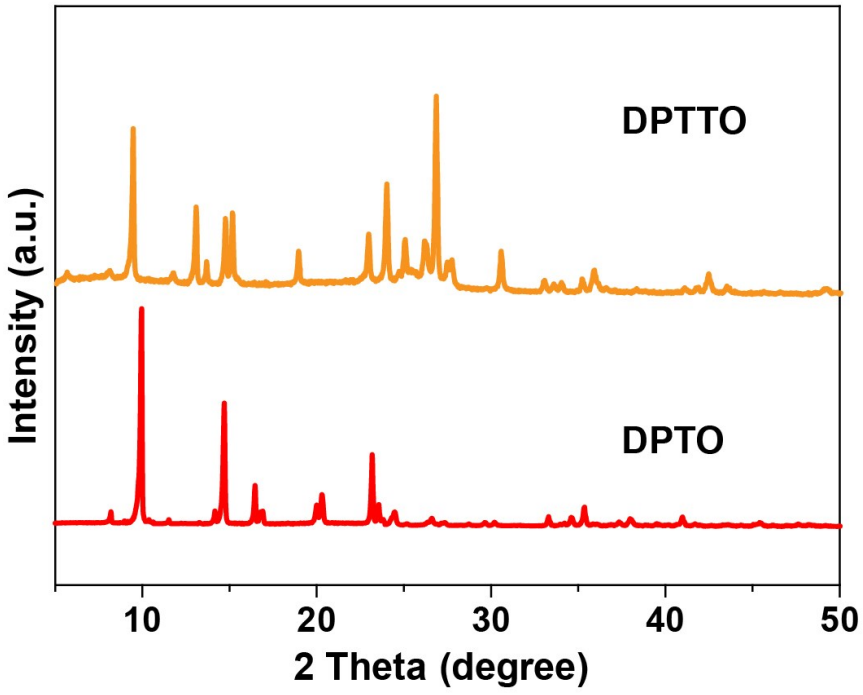

Figure S7. XRD patterns of **DPTO** and **DPTTO**.

7. SEM images

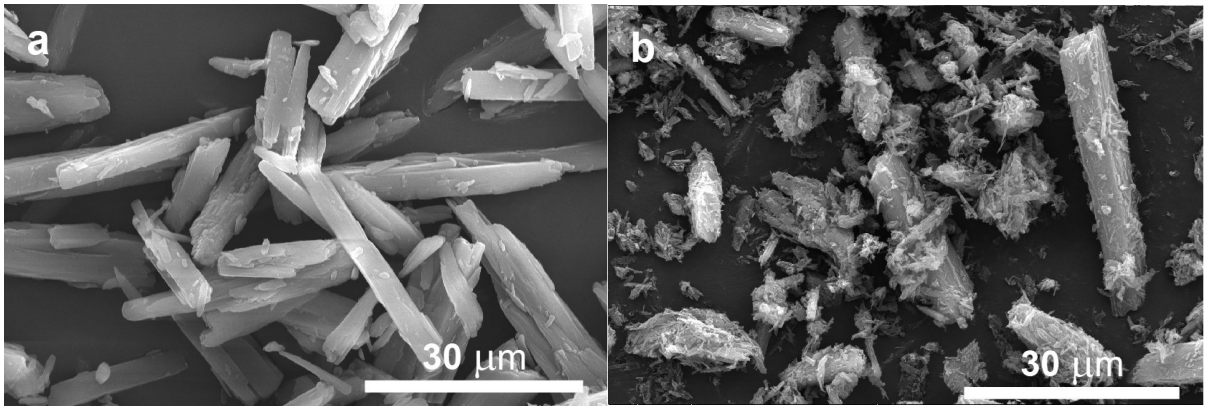

Figure S8. SEM images of (a) **DPTO** and (b) **DPTTO**. The scale bars of three images are 30 μm.

8. TGA curves

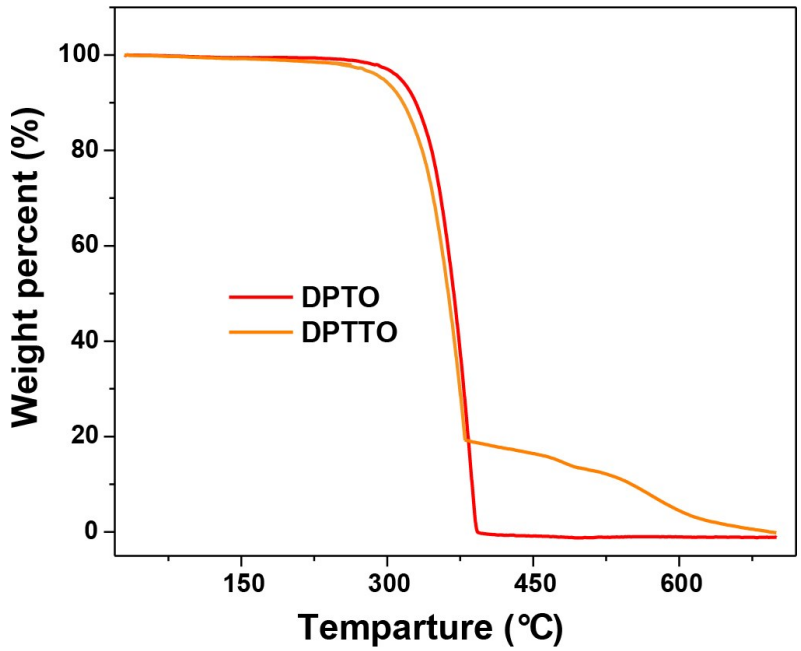

Figure S9. Thermogravimetric analysis plots of **DPTO** and **DPTTO.** The samples were heated at a rate of 10 °C min^{-1} in nitrogen. The thermal stability of the compounds is relatively good, with 5% weight loss occurring at 313 °C and 308 °C for **DPTO** and **DPTTO**, respectively. The Li-ion battery usually operates under room temperature; thus all the molecules are suitable candidates for electrodes.

9. Solubility experiments

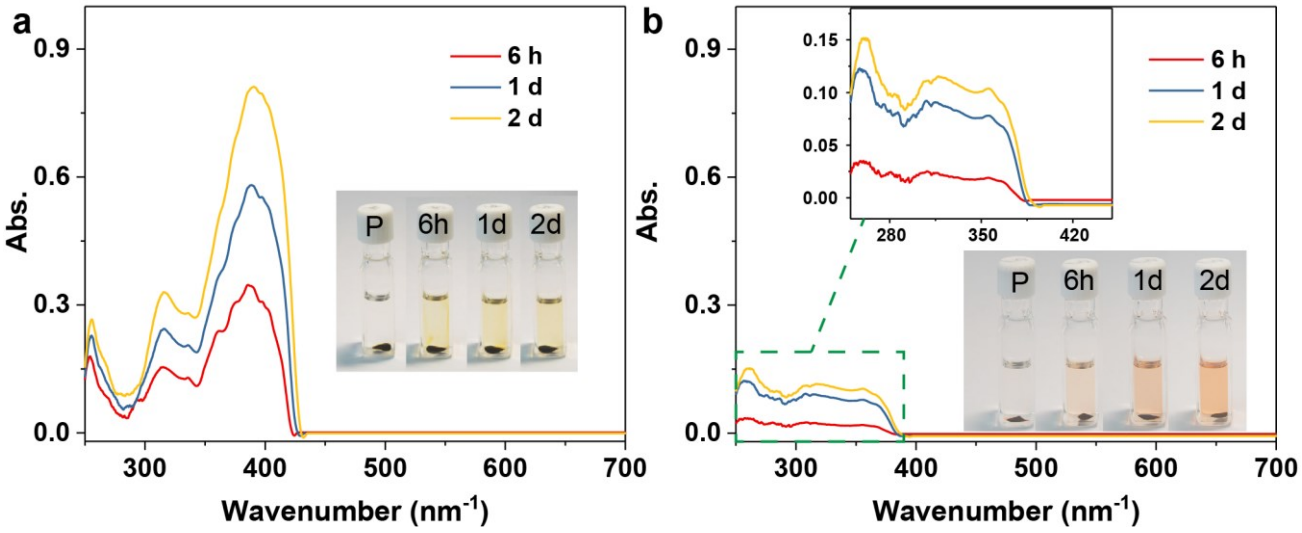

Figure S10. UV-vis spectra of solubility experiments with (a) **DPTO** and (b) **DPTTO** in 1M LiTFSI in DME: DOL = 1:1 Vol% electrolyte

10. Electric conductivities of two compounds

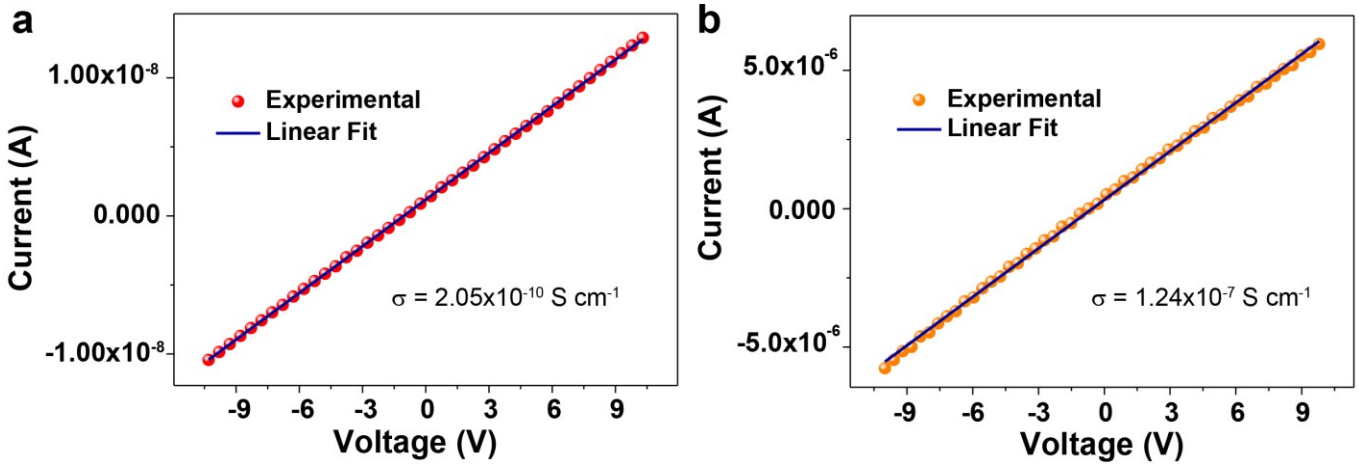

Figure S11. *I-V* curves of measurements for (a) **DPTO** and (b) **DPTTO**. The electrical conductivities were derived from the current−voltage (*I*−*V*) characterization curves at 25 °C under air. All samples were vacuum dried at 25 °C for 3 h before the measurements. The ground powder samples were pressed into Φ 6 mm pellets using a hand pellet press and sandwiched them between stainless steel pellet electrodes. The *I*−*V* curves were measured by sweeping voltages between −10 and +10 V. The electrical conductivity of each sample (σ) was calculated by the following equation:

$$\boldsymbol{\sigma} = \frac{\boldsymbol{LI}}{\boldsymbol{AV}} \quad (1)$$

where *L* is the distance between two electrodes, *I* is the current flow, *A* is the cross-sectional area of the sample, and *V* is the applied voltage.

11. Color of compounds

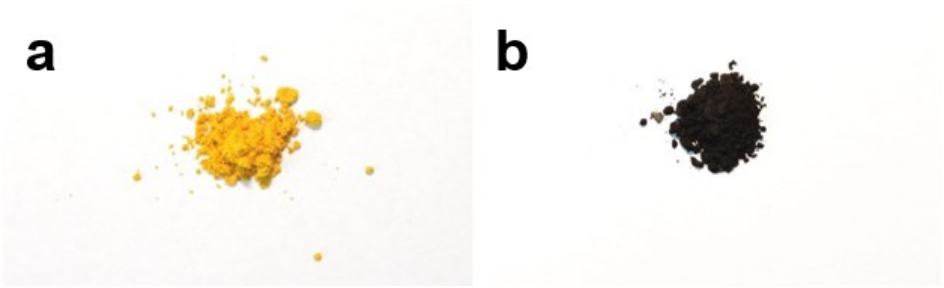

Figure S12. Digital photos of (a) **DPTO** and (b) **DPTTO** powder.

12. Battery Assembly and Tests

Half-cell assembly: Ketjen Black and PVDf were mixed with each compound to form slurry in weight ratio of 6/3/1. The mixed slurry was coated on the aluminium foil with a doctor blade, and then the electrode dried in a vacuum oven at 75 °C for 12 h. The whole piece of electrode sheet was cut into many circular pieces with area mass loading of ~1.0 mg cm^{-2}. The all process of electrodes assembly was carried in the glovebox under Ar atmosphere (H_2O and O_2 < 0.1 ppm, meanwhile). Lithium sheet is the counter electrode and reference electrode for the coin cell. The type of separator was Celgard3501 with 25 μL of electrolyte (1 M lithium bis-(trifluoromethanesulfonyl) imide (LiTFSI) in dimethyl carbonate (DME)/1,3-dioxolane (DOL) = 1/1 vol.%). The voltage range of all electrochemical performance measurement was 1.4−2.8 V with different current densities by using by a LANHE battery test station ((CT2001A, LANHE instruments, China) at 25 °C. It is important to note that the specific capacity of and the current density of the coin cells were calculated by the mass of the active material. Cyclic voltammograms (CV) were recorded by CHI660E electrochemical workstation (CH instruments Inc., U.S.A.) at different rate of 0.1, 0.2, 0.4, 0.6, and 0.8 mV s^{-1}. The electrochemical impedance analysis (EIS) was collected using an Autolab PGSTAT302N electrochemical workstation (Metrohm instruments Inc., Switzerland). The **DPTTO** electrode of *ex situ* X-ray powder diffraction (XRD) and *in situ* Raman measurements must soak the ionic liquid electrolyte, and therefore the mixture slurry was coated on circular aluminium foil with microporous. The equilibrium (open-circuit) potential of the cells is obtained by a galvanostatic intermittent titration technique (GITT), which consists of a series of current pulses at 0.25 C for 30 min, followed by a 6 h relaxation process. The open-circuit-voltage at the end of relaxation is considered to be the thermodynamically equilibrium potential.

13. Electrochemical results

Table S1. Theoretical capacities and utilization efficiencies of **DPTO** and **DPTTO**.

Compound	DPTO	DPTTO
Molecular weight	296.36	328.48
Theoretical Capacity (mAh g^{-1})	180.87	163.21
Capacity at 50 mA g^{-1} (mAh g^{-1})	162	163
Utilization Efficiency (%)	72.8%	98.2%

14. Calculated for Current contribution

Theoretically, the peaks can be divided into capacitive and diffusion components starting from the equation:

$$i = av^b \tag{2}$$

where *i* is the peak current, *v* is the scan rate, and *a* and *b* are parameters. The *b* value is the slope of the linear fit of a log(*v*) *vs.* log(*i*) plot. The cathodic and anodic slope values were calculated between 0.5~1, indicating that the charge storage mechanism was controlled by diffusion contribution and capacitive contribution. Furthermore, the contribution of the capacitive component at a specific scan rate was calculated according to the equation:

$$i = k_1 v + k_2 v^{\frac{1}{2}} \tag{3}$$

where $k_1 v$ corresponds to the pseudocapacitive contribution and $k_2 v^{\frac{1}{2}}$ represents the diffusion-controlled contribution.

15. Cyclic voltammogram and ln relationship of peak current and scan rate

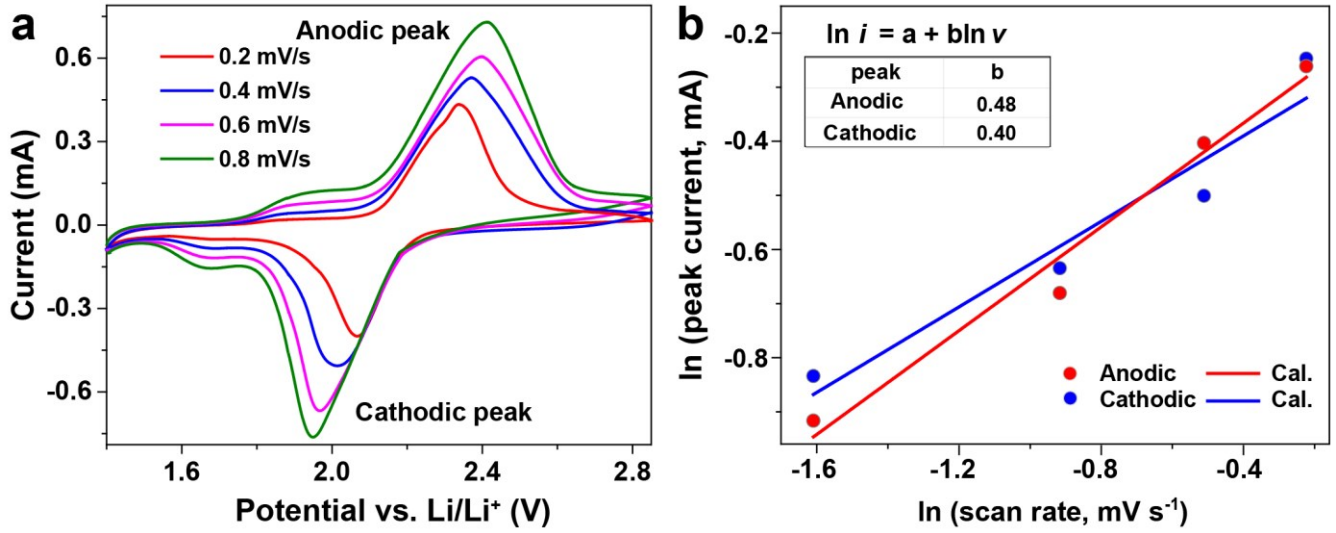

Figure S13. (a) Cyclic voltammetry scans from 0.2 to 0.8 mV s^{-1} of **DPTO**. (b) The ln relationship of peak current and scan rate for **DPTO**

16. EIS Nyquist plots and basic information

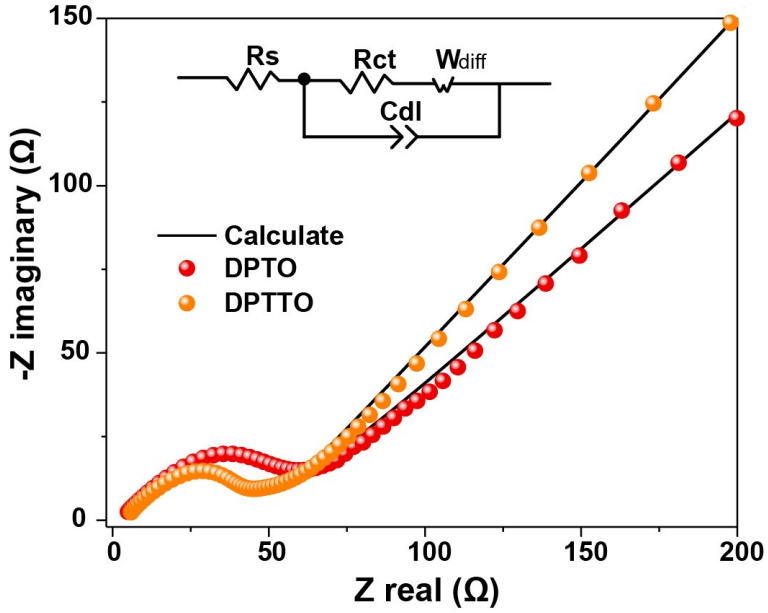

Figure S14. Nyquist plots of fresh **DPTO** and **DPTTO** cells. The inset shows the equivalent circuit including the values of electrolyte resistance (R_s), charge-transfer resistance (R_{ct}) and Warburg impedance (W_{diff}).

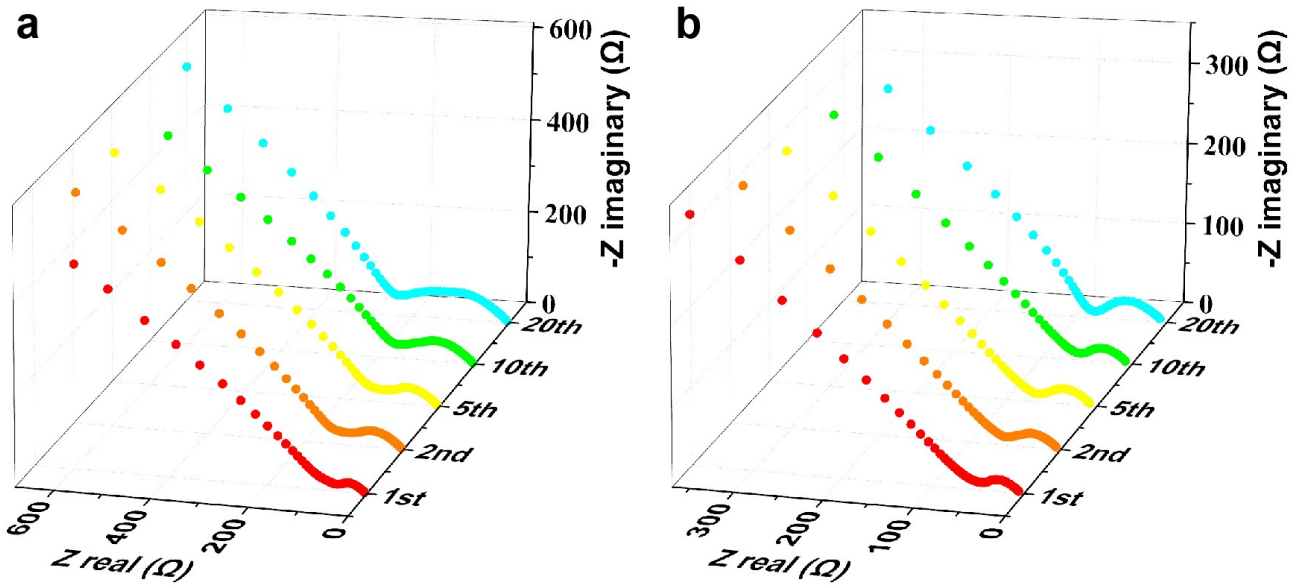

Figure S15. (a) and (b) Nyquist plots for **DPTO** and **DPTTO** cells obtained by electrochemical impedance spectroscopy tests at 1st, 2nd, 5th, 10th, and 20th cycling with fully charged states.

Table S2. The summary of R_{ct} (Ω) at different cycle number.

	Cycle number	1	2	5	10	20
R_{ct}	DPTO	55.7	110.5	148.7	196.3	267.2
	DPTTO	55.3	57.5	63.2	61.7	80.5

17. XPS survey

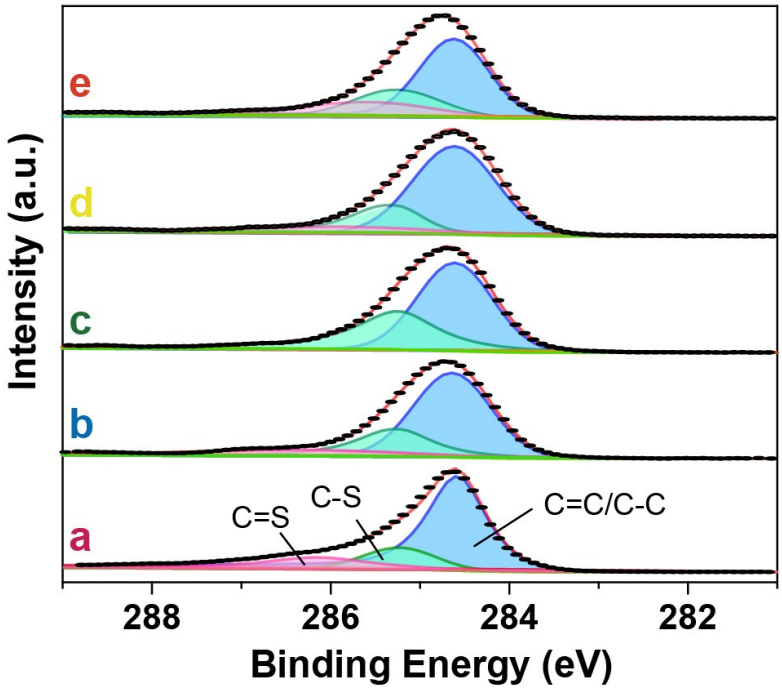

Figure S16. *Ex situ* XPS at marked points a-e in Figure 4a.

18. Density functional theory (DFT) calculation

All the quantum chemical calculations were achieved by Gaussian 09.[2] The calculated results of molecular electrostatic potential (MESP) was performed with Multiwfn 3.6 program.[3] After then, visual molecule dynamics (VMD) software visualized all the MESP plots.[4] Considering the Zero-point energy corrections, the M06-2X functional[5] and 6-311G(d,p) basis set were used to molecular geometry optimizations and frequency.

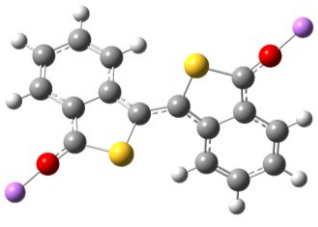	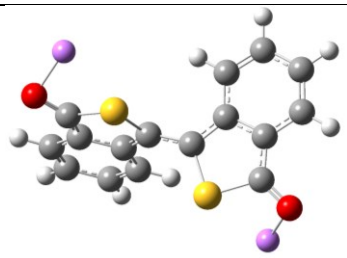
2Li case 1	2Li case 2
-1576.565	-1576.561

Figure S17. Possible molecular structures of Li_2- **DPTO** based on DFT calculations. Unit of energy (E): hartree.

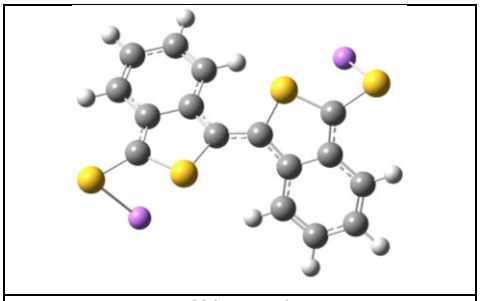

2Li case 1
-482.517

Figure S18. Possible molecular structure of Li_2- **DPTTO** based on DFT calculations. Unit of energy (E): hartree.

19. Redox mechanism of DPTO and DPTTO

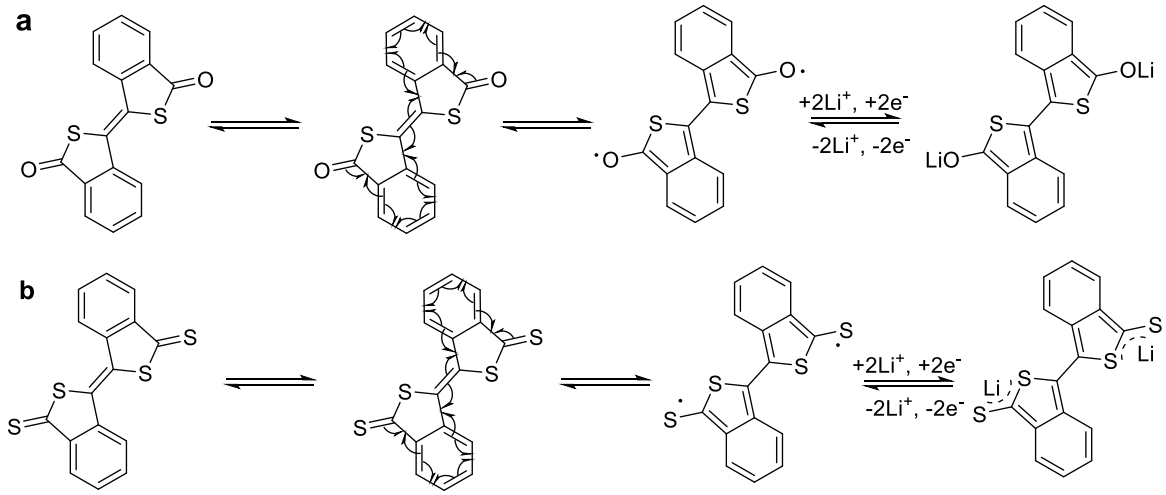

Figure S19. Proposed redox mechanism process of the a) **DPTO**. and b) **DPTTO** electrodes.

20. Flexible battery

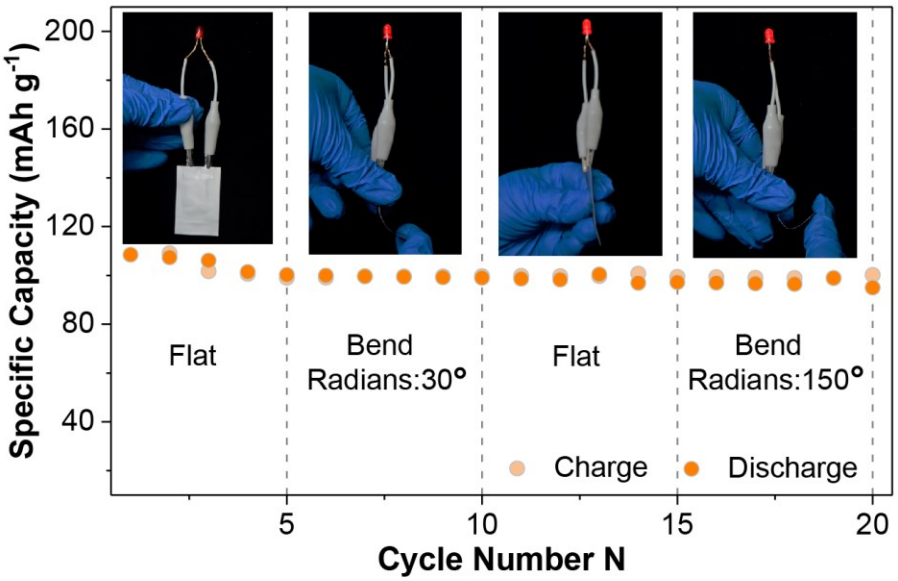

Figure S20. Cycling performance of the battery in the reciprocating flat and bend state.

21. Electrochemistry of Li_4-NaS_4TP half-cells

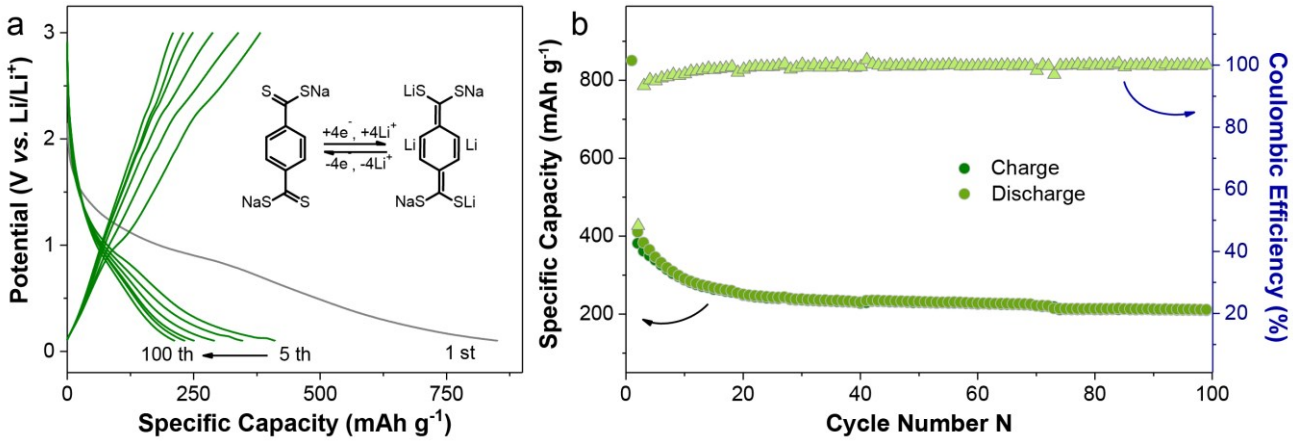

Figure S21. a) Potential-capacity profile at 50 mA g^{-1}. b) The corresponding capacity retention for 100 cycles.

22. Full-cell Assembly and Tests

$Li_2Na_2S_4TP$ electrodes: The reduced state ($Li_4Na_2S_4TP$) of Na_2S_4TP was introduced as anode. The preparation of the pristine Na_2S_4TP electrodes was as follows: Ketjen Black and PVdF were mixed with Na_2S_4TP powder to form a slurry in weight ratio of 6/3/1. The mixed slurry was coated on the copper foil with a doctor blade, and then the electrode dried in a vacuum oven at 60 °C for 12 h. The whole piece of electrode sheet was cut into many circular pieces with area mass loading of~1.1 mg cm^{-2}. The electrolyte is 1 M $LiPF_6$ in ethylene carbonate (EC)/dimethyl carbonate (DMC)/ethyl methyl carbonate (EMC) = 1:1:1 Vol%. After assembled coin cells, the Na_2S_4TP-based half-cells were discharged to 0.1 V. Next, the reduced state of Na_2S_4TP could be in situ formed $Li_4Na_2S_4TP$ in half cells. Full-batteries Assembly: The preparation procedure was like that mentioned above for half cells and the electrolyte is 1 M LiTFSI in DME/DOL

= 1/1 vol.% and 2 M LiTFSI in DME/DOL = 1/1 vol.%. Before the assemble process, the all electrodes in each half-cell was worked two cycles to clean up the unneeded side products of the pristine electrodes, respectively. The loading mass radio of $Li_4Na_2S_4TP$: **DPTTO** was about 1:2.5 (A/C ratio). Afterwards, the reduced-state $Li_4Na_2S_4TP$ and the DPTTO-based could be as a starting anode and cathode, respectively. The specific capacity and current density of the full-batteries were calculated based on the mass of cathode active material. The voltage range were 0.1-1.9 V and 0.1-2.0 V for $Li_4Na_2S_4TP$||DPTTO full cells.

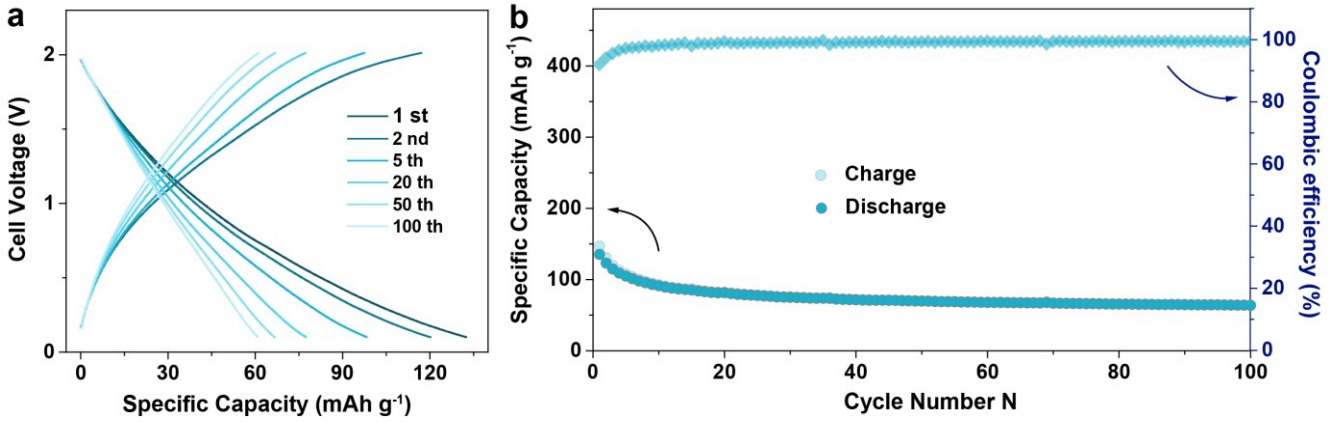

Figure S22 a) Galvanostatic charging/discharging of full-batteries. b) Cycle performance for the full-batteries.

Table S3. All organic Li-ion battery of small molecules.

Cathode	Anode	*V (V)*	C_{spec} (mAh g^{-1}) (stability)	Remarks	Ref.
BBQ	Li_4TP	1.7	60·(30%/1000·cycles)	High rate at 500 mA g^{-1}	6
ABB_4OLi	Li_2TP	1.8	70·(50%/200·cycles)	--	7
Li_4-PTtSA	Li_2-NDC	1.6	49 (60%/50 cycles)	--	8
Li4-PTtSA	ADALS	1.2	67 (60%/80 cycles)	--	8
Mg(Li_2)-*p*-DHT	Mg(Li_2)-*p*-DHT	0.8	140 (25%/20 cycles)	symmetrical	9
$Li_4C_8H_2O_6$	$Li_6C_8H_2O_6$	1.8	214 (95%/50 cycles)	symmetrical	10
DPTTO	Li_4-Na_2S_4TP	0.65	75 (60%/100·cycles)	All rich-sulfur electrode	This work

23. Reference

1. L.-Y. Wang, G.-G. Gu, T.-J. Yue, W.-M. Ren and X.-B. Lu, *Macromolecules*, 2019, **52**, 2439-2445.
2. M. J. Frisch, G. W. Trucks, H. B. Schlegel, G. E. Scuseria, M. A. Robb, J. R. Cheeseman, G. Scalmani, V. Barone, G. A. Petersson, H. Nakatsuji, X. Li, M. Caricato, A. V. Marenich, J. Bloino, B. G. Janesko, R. Gomperts, B. Mennucci, H. P. Hratchian, J. V. Ortiz, A. F. Izmaylov, J. L. Sonnenberg, Williams, F. Ding, F. Lipparini, F. Egidi, J. Goings, B. Peng, A. Petrone, T. Henderson, D. Ranasinghe, V. G. Zakrzewski, J. Gao, N. Rega, G. Zheng, W. Liang, M. Hada, M. Ehara, K. Toyota, R. Fukuda, J. Hasegawa, M. Ishida, T. Nakajima, Y. Honda, O. Kitao, H. Nakai, T. Vreven, K. Throssell, J. A. Montgomery Jr., J. E. Peralta, F. Ogliaro, M. J. Bearpark, J. J. Heyd, E. N. Brothers, K. N. Kudin, V. N. Staroverov, T. A. Keith, R. Kobayashi, J. Normand, K. Raghavachari, A. P. Rendell, J. C. Burant, S. S. Iyengar, J. Tomasi, M. Cossi, J. M. Millam, M. Klene, C. Adamo, R. Cammi, J. W. Ochterski, R. L. Martin, K. Morokuma, O. Farkas, J. B. Foresman and D. J. Fox, *Journal*, 2009.
3. T. Lu and F. Chen, *J. Comput. Chem.*, 2012, **33**, 580-592.
4. W. Humphrey, A. Dalke and K. Schulten, *J. Mol. Graph.*, 1996, **14**, 33-38.
5. Y. Zhao and D. G. Truhlar, *Theor. Chem. Acc.*, 2007, **120**, 215-241.

6. Z. Yao, W. Tang, X. Wang, C. Wang, C. Yang and C. Fan, *J. Power Sources*, 2020, **448**, 227456.
7. Y. Hu, W. Tang, Q. Yu, C. Yang and C. Fan, *ACS Appl. Mater. Interfaces*, 2019, **11**, 32987-32993.
8. J. Wang, A. E. Lakraychi, X. Liu, L. Sieuw, C. Morari, P. Poizot and A. Vlad, *Nat. Mater.*, 2021, **20**, 665-673.
9. A. Jouhara, N. Dupré, A.-C. Gaillot, D. Guyomard, F. Dolhem and P. Poizot, *Nat. Commun.*, 2018, **9**, 4401.
10 S. Wang, L. Wang, K. Zhang, Z. Zhu, Z. Tao and J. Chen, *Nano Lett.*, 2013, **13**, 4404-4409.